ORIGINAL ARTICLE

lajss.org
Latin American Journal of Solids and Structures

www.lajss.org

The application of refractory high entropy alloys in shaped charge

Yuanchen Wang[a], Xudong Zu[a*], Zhengxiang Huang[a], Qiangqiang Xiao[a], Xin Jia[a]

[a] School of Mechanical Engineering, Nanjing University of Science and Technology, Nanjing 210094, China. Email: 1003900530@qq.com, zuxudong9902@njust.edu.cn, huangyu@mail.njust.edu.cn, xiao_wawj@njust.edu.cn, jiaxin@mail.njust.edu.cn

* Corresponding author

https://doi.org/10.1590/1679-7825/e8579

Abstract

High entropy alloys (HEAs) have attracted widespread attention from researchers as emerging materials. Among them, refractory high entropy alloys (RHEAs) have shown potential for application in high-temperature environments due to their excellent high-temperature mechanical properties. This study mainly focuses on TiAlVZrNb RHEAs, conducting quasi-static and dynamic mechanical experiments, and fitting Johnson Cook constitutive equation parameters. In addition, the formation and aftereffect of the jets are studied through experiments. The temperature and yield strength distribution of the jets are studied through numerical simulation. The results indicate that under quasi-static loading, TiAlVZrNb RHEAs exhibit high yield strength and excellent ductility. The cohesiveness of the jet is discussed by combining the theoretical and mechanical properties. The burn marks on the quilt and oil tank behind the target also confirm the strong aftereffect of TiAlVZrNb RHEAs jet. This study can provide a reference for the application and design of RHEAs liner.

Keywords

TiAlVZrNb RHEAs, Mechanical properties, Shaped charge, Jet formation, Jet cohesiveness

Graphical Abstract

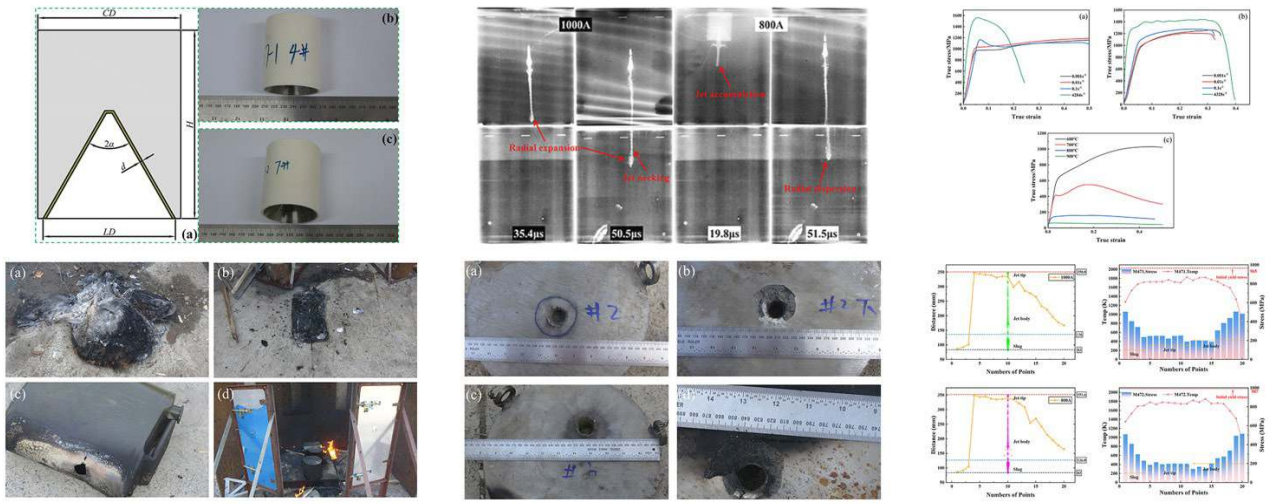

Received February 25, 2025. In revised form April 21, 2025. Accepted May 10, 2025. Available online May 21, 2025.
https://doi.org/10.1590/1679-7825/e8579

Latin American Journal of Solids and Structures. ISSN 1679-7825. Copyright © 2025. This is an Open Access article distributed under the terms of the Creative Commons Attribution License, which permits unrestricted use, distribution, and reproduction in any medium, provided the original work is properly cited.

1 INTRODUCTION

As an important research direction in the field of explosion mechanics, the core principle of shaped charge technology is to form high-speed jet through the directional release of explosive explosion energy to achieve efficient target damage. It has demonstrated irreplaceable application value in military armor penetration (Cai, Y. E. et al. 2024, Reboul, N. et al. 2025), oil extraction (Kong, C. et al. 2024), electromagnetic pulse (Guo, J. et al. 2024) and other fields. Among them, liner is the key functional component of shaped charge, and its material characteristics are one of the core factors that determine the ability of jet damage.

With advancements in material science and breakthroughs in preparation technology, an increasing number of materials have been developed and utilized in shaped charges. Related studies have shown that compared to high-density jets such as copper, titanium alloy jets and aluminum alloy jets have higher tip velocities and higher hole-expansion efficiency (Zhang X. W. et al. 2020, Guo J. et al. 2017, Niu Y. Q. et al. 2024). In addition, amorphous alloy liner can form non-cohesive jets, and radial dispersion will increase the jet diameter and improve the hole-expansion efficiency (Shi J. et al. 2023a, Han J. et al. 2019, Shi J. et al. 2022, Shi J. et al. 2023b). In particular, reactive material jets have higher hole-expansion efficiency due to their unique energy release characteristics (Guo H. G. et al. 2022, Wang H. et al. 2019, Sun T. et al. 2024, Zheng Y. et al. 2023).

Since the first proposal in 2004 (Yeh J. W. et al. 2004, Cantor B. et al. 2004), HEAs as an emerging material, have gradually gained widespread concern due to innovative concepts and excellent physical and chemical properties. Among them, refractory high entropy alloys (RHEAs) mainly composed of refractory metal elements have excellent high-temperature mechanical properties and greater application potential. Senkov et al. (2010,2011) first prepared MoNbTaW and MoNbTaVW RHEAs. Although the yield strength is high, their limited ductility at room temperature is only 2% and 1.5% of plastic strain, respectively. Body centered cubic (BCC)RHEAs have high yield strength at both room temperature and high temperature, but they have high brittleness and density, which limits its application. Replacing high-density metal elements (Ta, Hf, W) with lightweight elements (Al, Mg, Li, Ti) makes the design of lightweight high entropy alloys (LHEAs) diverse (Wang X. et al. 2022, Yurchenko N Y. et al. 2017). Among them, TiAlVZrNb RHEAs have extremely high application potential due to its advantages of low density, high strength, and high ductility (Wang X. et al. 2022, Wang L. et al. 2021, Li T. et al. 2025).

At present, a few researchers have conducted experimental and numerical simulation studies on HEAs liner. Based on numerical simulation, Yan et al. (2022) study the fracture law during the jet tension of CrMnFeCoNi five element HEAs to find that the fracture time is negatively correlated with the dynamic strength of the material. Chen et al. (2022) analyze the microstructure of residual jet in CoCrNi medium entropy alloys (MEAs) and find that dynamic recrystallization (DRX) occurs during the formation of the jet. However, the Cr-rich BCC reduces the ductility and penetration ability of the jet. Li et al. (2024) investigate the different deformation mechanisms of CoCrFeNi HEAs at different strain rates. In addition, CoCrFeNi HEAs jet exhibits excellent hole expanding ability during the penetration process of C45 steel targets. LIU et al. (2024) design a shaped charge structure and verify the penetration capability of CoCrFeNiTi LHEAs through numerical simulation and experiment. Wang et al. (2025) find that DRX of BCC phase and α2 phase occurred in the recovered slug of Ti-Zr-Nb-Al Precipitation-hardened high entropy alloys (PHEAs). The deformation of α2 phase is later than that of BCC phase, which increases the deformation resistance. The above studies have focused on the penetration ability of HEAs jet and deformation characteristics of slug. However, the penetration ability of the jet depends on the shape of the jet, and the temperature of the jet is also one of the important factors affecting the shape of the jet. Therefore, it is necessary to further study jet formation and jet temperature distribution.

Compared to traditional HEAs, TiAlVZrNb RHEAs are more suitable as liner materials. The low density of the material increases the velocity of jets. The Ti, Al, and Zr elements in the RHEAs increase the possibility of radial dispersion and gives the jet energy release characteristics (Ren K. et al. 2021). Therefore, it is necessary to study the application of TiAlVZrNb RHEAs in liner materials. This study takes TiAlVZrNb RHEAs as the research object. The constitutive parameters applicable to TiAlVZrNb RHEAs are obtained through quasi-static and dynamic mechanical tests. A numerical simulation model is established based on the structure of the shaped charge. The accuracy of constitutive parameters is verified through numerical simulation, and the stress and temperature distribution as well as the evolution of head morphology during jet formation are studied. The cohesion of the jet is predicted through theory model. In addition, the aftereffect of jet has been verified.

2 MATERIALS AND TESTS PREPARATION

2.1 X-ray experiments

Previous studies have shown that the shape of the jet is directly related to the liner materials, therefore it is necessary to study the jet formation. X-ray experiments are one of the most effective methods for studying jet formation. The X-ray equipment consists of two ray generators and two films. According to the emission time, the shape of the jet will be recorded in the photos.

In this study, experiments are designed and conducted using a diameter of Ø56mm shaped charge (SC) structure, as shown in Figure 1. The 400g TiAlVZrNb ($Ti_{55}Al_{20}V_5Zr_5Nb_{15}$) non-equiatomic HEAs ingot is prepared by vacuum floating melting Ti, Zr, V, Nb, Al metals with high purity (>99.9wt%) in a water-cooled copper crucible with a diameter of 60 mm and height of 60 mm under protection of Argon, and the ingots are melted at least three times to obtain elements homogenous ingots. The ingot is annealed at 1000 °C and then water-cooled to obtain a single BCC phase structur and annealed at 800 °C and then water-cooled to obtain an "α2+BCC" dual phase structure (Wang X. et al. 2022). The SC consists of a main charge and TiAlVZrNb RHEAs liners. The liner materials contain two kinds of RHEAs with different phase structures, which are BCC single-phase(1000A) and “BCC+α2” dual phase(800A). The main charge is 8701 explosives, which is detonated through the center of the detonator at the bottom. The diameter of SC (*CD*) is Ø56mm and the height of SC(*H*) is 73.3mm. The cone angle(2*α*) is 60 °, the thickness of the liner (*d*) is 1mm, and the diameter of the mouth (*LD*) is 54.15mm. Figure 1 is the picture of the SC.

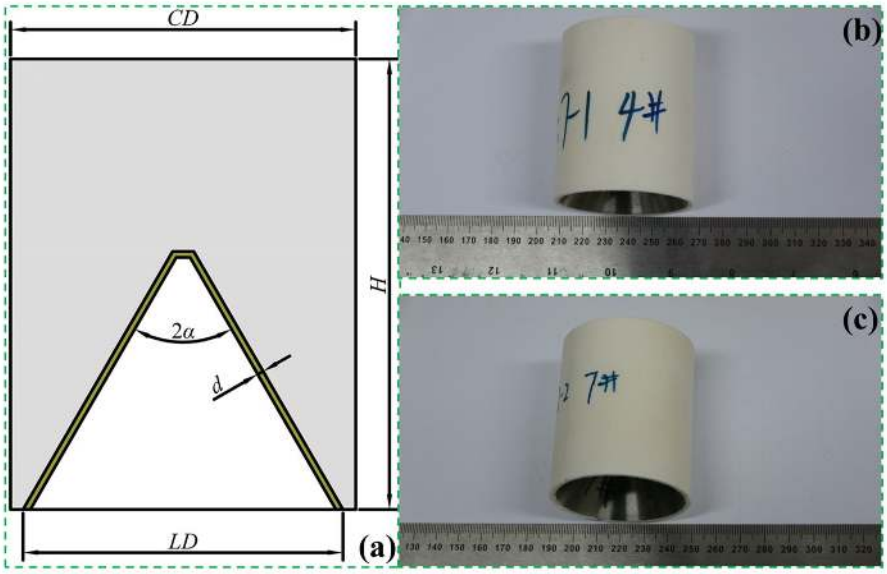

Figure 1 Structure and photos of SCs: (a) Structure of the SCs (b) 1000A SC photo (c)800A SC photo.

The report conducts experiments by using the Swedish Scandiflash X-ray machine. The SC is hung in the center of the field of view. Before the experiments, the distances are measured to calculate the magnification ratio. The X-ray emission time T_1 and T_2 are set to 10μs and 40μs, respectively. The tip velocity and tail velocity can be calculated by magnification ratio and emission time. The X-ray experimental setup is shown in Figure 2.

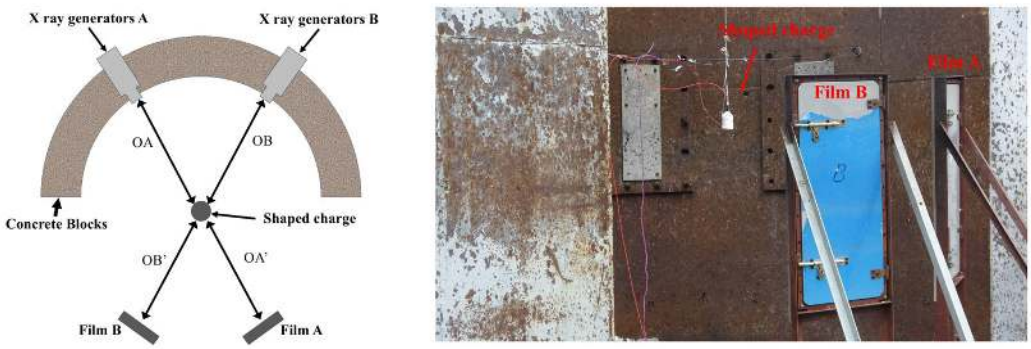

Figure 2 X-ray experiments setup.

The magnification ratio k_a and k_b can be expressed as:

$$\begin{cases} k_a = OA / (OA' + OA) \\ k_b = OB / (OB' + OB) \end{cases} \tag{1}$$

where OA and OB are the distances between the shaped charge and the X-ray generators. OA' and OB' are the distances between the SC and the X-ray film A and film B.

The tip velocity V_J and tail velocity V_S are expressed as:

$$\begin{cases} V_j = (L_{tipB} / k_b - L_{tipA} / k_a) / \triangle t \\ V_s = (L_{tailB} / k_b - L_{tailA} / k_a) / \triangle t \end{cases} \tag{2}$$

where $\Delta t = T_2 - T_1$ is the time difference between taking two photos. L_{tipB} and L_{tipA} are the distances from the jet tip to the marked line in film B and film A, respectively. L_{tailB} and L_{tailA} are the distances from the jet tail to the marked line in film B and film A, respectively.

2.2 Aftereffect experiments

To investigate the aftereffect of RHEAs jets, experiments are designed and conducted. In the experiments, a 30mm 45# steel target is hung by iron wire at 1.3m from the ground and is level. An oil tank and quilt are placed below the 45#steel target to verify the aftereffect of the jet. After the jet penetrates the steel target, the jet and fragments will damage the oil tank and quilt. At the same time, X-rays will take photos at the corresponding time. The T_1 and T_2 are set to 35μs and 90μs, respectively. The aftereffect experimental setup is shown in Figure 3. The experimental data is shown in the Table 1. H_1 is the distance between shaped charge and 45#steel. H_2 is the distance between 45#steel and combustible. P is the distance between the combustible and the centerline. *B* is the thickness of the 45#steel.

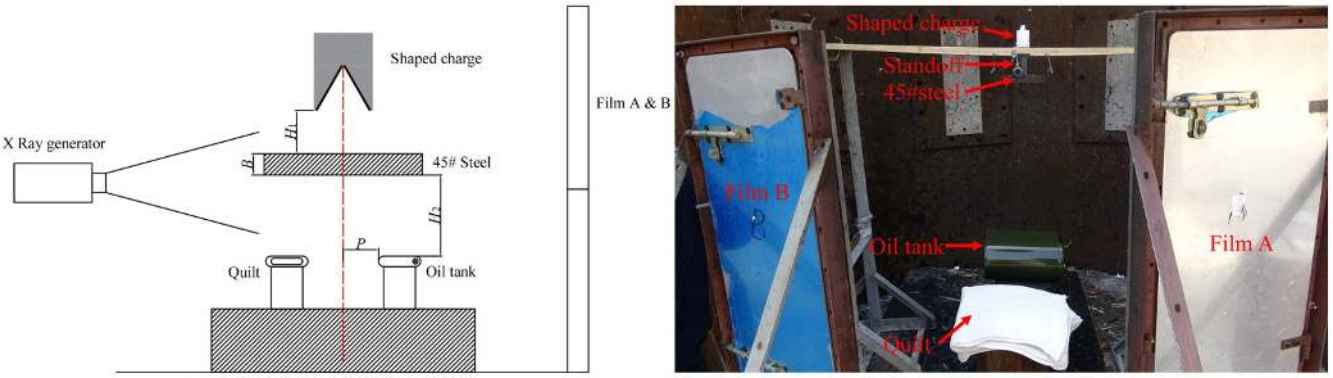

Figure 3 Aftereffect experiments setup.

Table 1 Aftereffect experimental data.

Materials	P/mm		H_1/mm	H_2/mm	B/mm
	Oil tank	quilt			
1000A	80	60	120	750	30
800A	40	60	120	750	30

2.3 Mechanical properties texts

The quasi-static compression texts and dynamic compression texts are carried out at room temperature. The quasi-static compression tests are conducted three times, and the strain rates are 0.001 s^{-1}, 0.01 s^{-1} and 0.1 s^{-1} respectively. The size of the sample is 4mm in diameter and 6mm in height. Dynamic compression tests are performed by a split-

Hopkinson pressure bar (SHPB) at strain rates of ~$10^3 s^{-1}$ on specimens with a diameter of 4 mm and height of 4 mm. In addition, high temperature compression texts at different temperatures of 1000A are carried out, and the strain rate is set to 0.001 s^{-1}.

3 RESULTS OF MECHANICAL PROPERTIES TESTS

3.1 Mechanical properties of TiAlVZrNb RHEAs

Figure 4 (a) and (b) show the compression curves of TiAlVZrNb RHEAs. At the strain rate of 0.001s^{-1}, the 1000A shows a yield strength $\sigma_{0.2}$=965MPa and maximum strength σ_m=1150MPa. When the true strain reaches 20%, 1000A shows strain hardening. It is worth noting that the plastic strain of 1000A exceeds 50% under quasi-static conditions and no shear fracture occurs (Wang X. et al. 2022). As the strain rate increases from 0.001s^{-1} to 0.1s^{-1}, yield strength slightly increases to 1170MPa and still does not fracture. At the strain rate of 0.001s-1, the 800A shows a yield strength $\sigma_{0.2}$=985MPa and maximum strength σ_m=1260MPa. At strain rates of 0.001s^{-1}, 0.01s^{-1}, and 0.1s^{-1}, the increasing trend of flow stress at 800A is similar, and fracture strain is about 31%. However, significant changes occur at the strain rate of $4\times10^3 s^{-1}$. The maximum stress strength of 1000A rapidly increases from 965MPa to 1555MPa, but the fracture strain sharply decreases to about 20%. Compared with 1000A, 800A shows a synergistic increase in ductility and strength, with the maximum stress strength of 1440MPa and the fracture strain of approximately 37%. Figure 4 (c) shows the 1000A compression curves at different temperatures. As the temperature increases from 600°C to 900°C, the yield strength of 1000A decreases from 619MPa to 54MPa. Yield strength is negatively correlated with temperature。

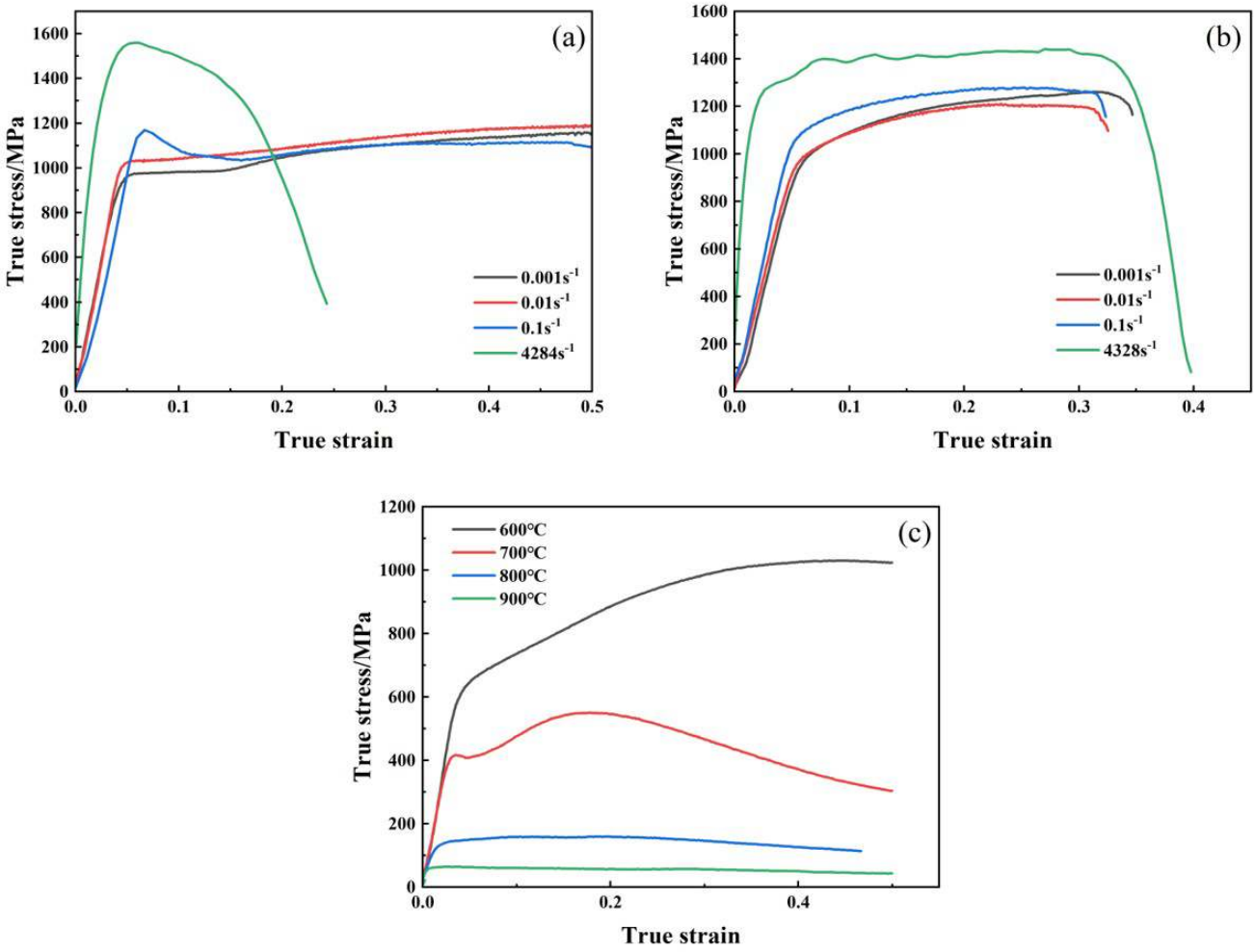

Figure 4 Compression curves of TiAlVZrNb RHEAs: (a) 1000A compression curves at different strain rates (b) 800A compression curves at different strain rates (c) 1000A compression curves at different temperatures.

3.2 Johnson-Cook constitutive parameters fitting

The Johnson Cook model is generally used to predict the flow stress of materials undergoing large deformation under high strain rates and high temperature and widely used in the study of dynamic mechanical properties and impact dynamics of metals (Chen C. et al. 2023).

The basic form of Johnson Cook constitutive model is (Johnson,1983):

$$\sigma_y = \left(A + B\varepsilon_p^n\right)\left(1 + C\ln\dot{\varepsilon}_p\right)\left(1 - T^{*m}\right) \tag{3}$$

$$T^* = \frac{T - T_{ref}}{T_{melt} - T_{ref}} \tag{4}$$

where σ_y is the Von Mises equivalent stress; ε_p is the equivalent plastic deformation; $\dot{\varepsilon}_p = \dot{\varepsilon} / \dot{\varepsilon}_0$ is the normalized effective plastic strain rate; $\dot{\varepsilon}_0$ is the reference strain rate; A is the initial yield strength; B is the hardening modulus; n is the stress hardening exponent; C is the strain rate hardening coefficient; m is the thermal softening coefficient; T is the current temperature, T_{melt} is the melting temperature and T_{ref} is the reference temperature.

When the current temperature $T = T_{ref} = 293\mathrm{K}$, strain rate $\dot{\varepsilon} = \dot{\varepsilon}_0 = 0.001\mathrm{s}^{-1}$, Eq.(4) can be simplified and applies logarithmic variation:

$$\ln\left(\sigma_y - A\right) = n\ln\varepsilon_p + \ln B \tag{5}$$

When the current temperature $T = T_{ref} = 293\mathrm{K}$, strain rate $\dot{\varepsilon} \neq \dot{\varepsilon}_0$, Eq. (4) can be simplified as:

$$\sigma_y \Big/ \left(A + B\varepsilon_p^{\ n}\right) = C\ln\dot{\varepsilon}^* + 1 \tag{6}$$

When the strain rate $\dot{\varepsilon} = \dot{\varepsilon}_0 = 0.001\mathrm{s}^{-1}$, $T \neq T_{ref}$, Eq. (4) can be simplified as:

$$m\ln T^* = \ln\left[1 - \frac{\sigma_y}{\left(A + B\varepsilon_p^n\right)}\right] \tag{7}$$

According to the quasi-static texts results, the initial yield strength *A* are 965MPa and 987MPa. Parameters B and n are fitted by using Eq.(5). Parameter C is fitted by using Eq.(6) based on the initial yield strength of RHEAs at different strain rates. Fitting results are show in Figure 5 and Table 2. According to the texts results at different temperatures, Eq.(7) is used to fit the parameter m. Since 800A has not been subjected to different high temperature compression tests, the same parameter m is used for numerical simulation as 1000A.

Table 2 Parameters of 1000A and 800A.

Materials	ρ/(g/cm³)	A/MPa	B/MPa	n	C	m	T_{melt}/K
1000A	4.70	965	450	0.97	0.0215	0.6	1943
800A	4.70	985	742	0.62	0.0203	0.6	1943

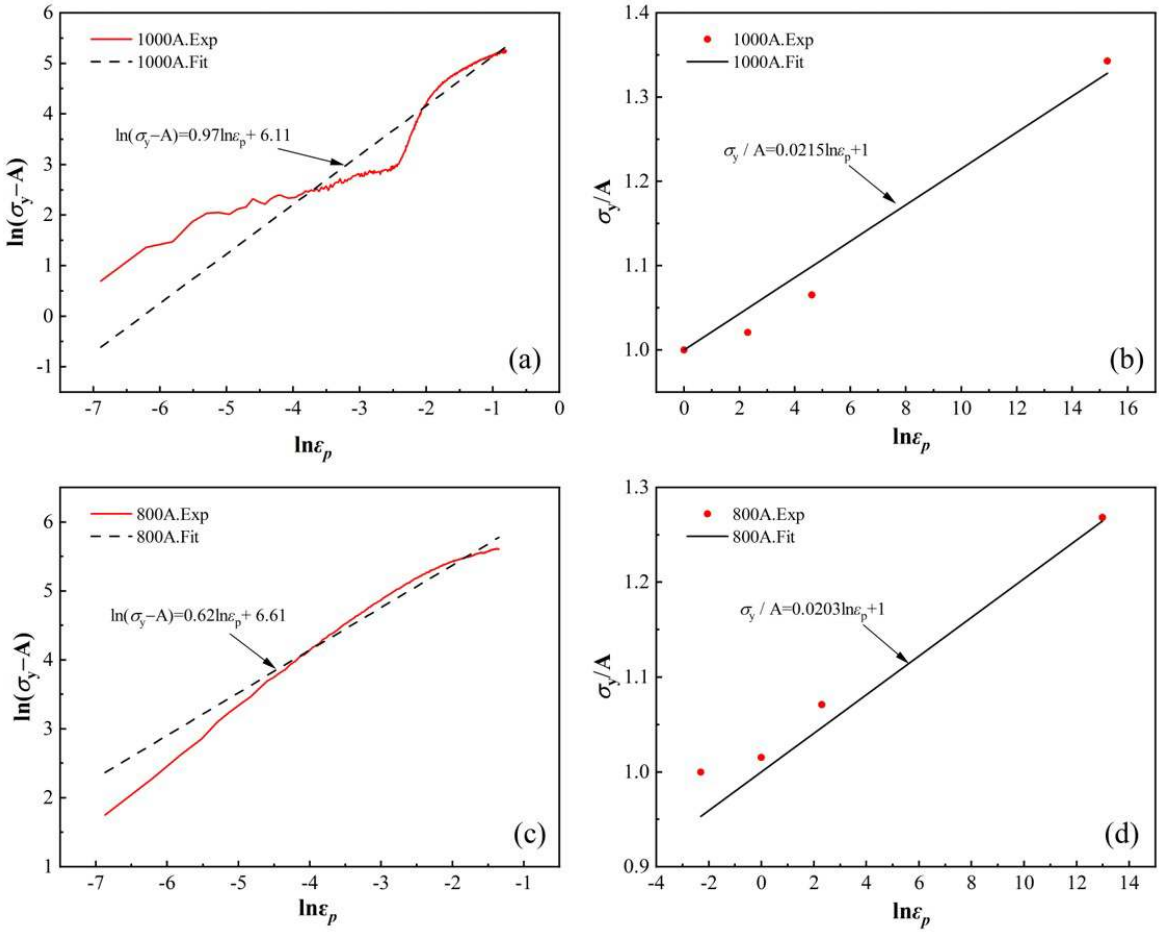

Figure 5 Johnson-Cook parameters fitting: (a) Parameter B & n fitting of 1000A (b) Parameter C fitting of 1000A (c) Parameter B & n fitting of 800A (d) Parameter C fitting of 800A.

4 RESULTS AND DISCUSSION

4.1 X-ray experiments results

According to the experimental setup, X-ray experiments are conducted to obtain the morphology of jet at two time points. Two sets of photos are taken in the X-ray experiments, as shown in Figure 6. Due to equipment and weather conditions, there is a deviation between the actual shooting time of the two experiments and the emission time.

At 35.4μs, the 1000A liner has undergone a collapse. The head of the 1000A jet is approximately elliptical in shape, and small cavities can be found inside the jet head. At 50.5μs, an increase in the volume and number of cavities lead to an increase in the volume of the jet head. Although the jet head shows radial expansion, necking caused by jet tension can still be observed. At 19.9μs, the 800A jet does not show serious non-cohesiveness, and no cavities are observed in the jet head. With the increase of time(51.5μs), the 800A jet head shows radial dispersion obviously. Unlike 1000A jet, radial dispersion leads to the disappearance of the necking.

Under certain resolution conditions, the particles concentration and dispersion around the jet head in photos reflect the non-cohesiveness of the jet. The experimental results show that in the end stage of jet formation, the material particles near the jet head are more dispersed, while the material particles at the slug and tail are more concentrated and brighter. It means that radial dispersion may first occur at the head of the jet. In the collapse stage, the deformation of the liner depends on the plastic deformation of the material. At extremely high strain rates, the deformation mechanism of materials mainly manifests as adiabatic shear (Dirras, G. et al. 2016, Lee, W. S. et al. 2007). Compared to 1000A, the second phase particles distributed in 800A may hinder dislocation slip, which is beneficial for improving dynamic plasticity. The high temperature accumulated by plastic deformation can further cause strain softening of 1000A material after yielding. Poor dynamic plasticity may reduce the cohesiveness of the jet (Shi J. et al. 2023b). Compared

with 1000A, 800A has better dynamic plasticity, so radial dispersion first occurs on the outer side of the jet head. On the contrary, cavities first appear in the head of the 1000A jet.

Table 3 shows the experimental results for the TiAlVZrNb RHEAs jet. The velocity of the 1000A jet is approximately 6982.1m/s, slightly higher than the 800A jet. The diameter of the jet head at T_2 is greater than that at T_1, which also proves that the cohesion of the jet is poor. L_J is the length from jet tip to jet tail; D_J is the diameter of the jet head.

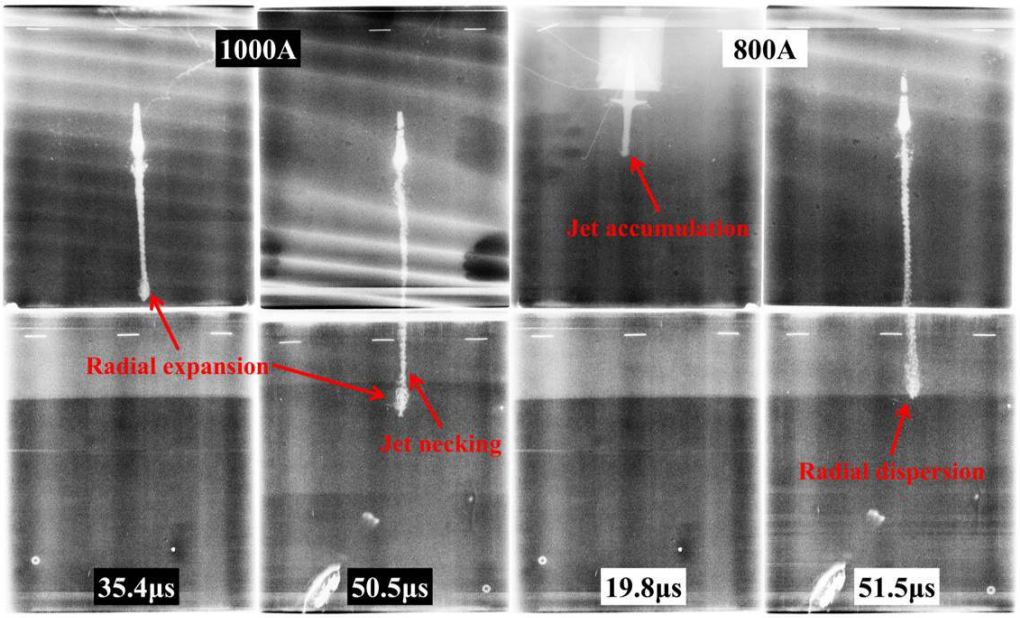

Figure 6 Jet morphology of TiAlVZrNb RHEAs at different times.

Table 3 Experimental results of TiAlVZrNb RHEAs jet.

Materials	T_1/μs	T_2/μs	L_J/mm		D_J/mm		V_J/(m/s)
			T_1	T_2	T_1	T_2	
1000A	35.4	50.5	111.3	209.1	7.98	11.0	6982.1
800A	19.9	51.5	39.6	228.4	5.23	10.8	6666.2

4.2 Aftereffect experiments results

The shape of the jet penetrating the target plate can be predicted by the number and size of craters on the 45# steel targets. If there is severe radial dispersion at the jet head, multiple craters of varying sizes can be observed on the 45# steel target, and the craters will be widely distributed on the impact surface (Shi J. et al. 2023a). In both experiments, there is a visible penetration hole on the surface of the steel target, indicating the good shape of the jet before penetrating the target. In addition, the back of the steel target is subjected to the combined effect of tensile waves and shock waves, resulting in a large area of collapse. Figure 7 shows the damage of the steel targets. The hole-expanding efficiency of the two types of jets on the 45 # steel target at a height of 120mm is similar, but the diameter of the hole after the 800A jet penetrates the steel target is slightly smaller, and the collapse area on the back of the target is larger. Table 4 shows the aftereffect experimental results. D_1 is the diameter of the inlet hole. D_2 is the diameter of the outlet hole. D_3 is the diameter of the collapse area.

Table 4 Aftereffect experimental results.

Materials	D_1/mm	D_2/mm	D_3/mm
1000A	34(0.60CD)	26(0.46CD)	53
800A	35(0.62CD)	22.4(0.40CD)	59

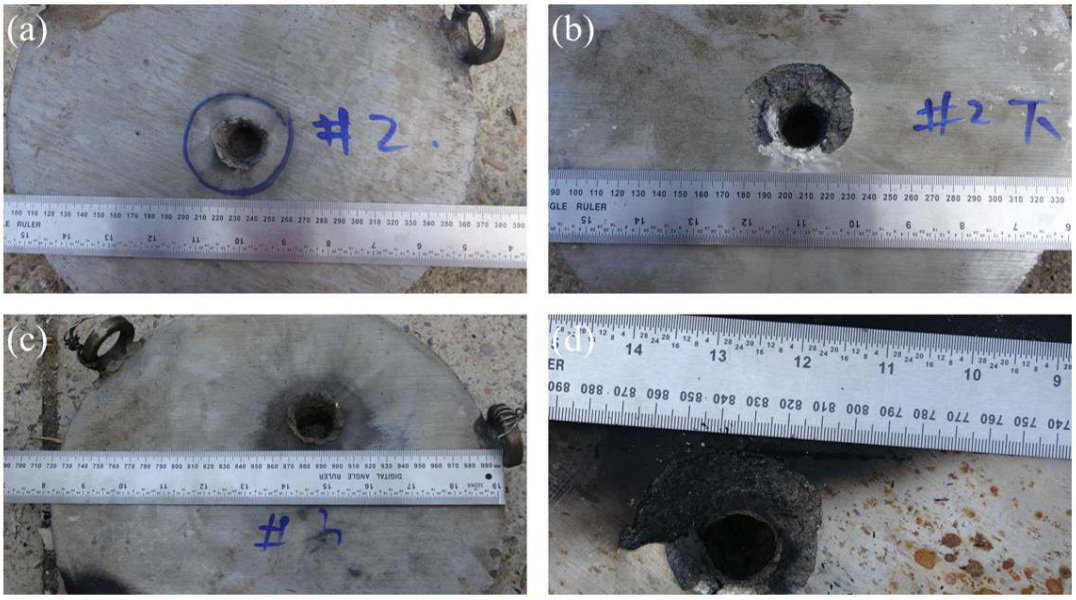

Figure 7 Damage of steel targets.

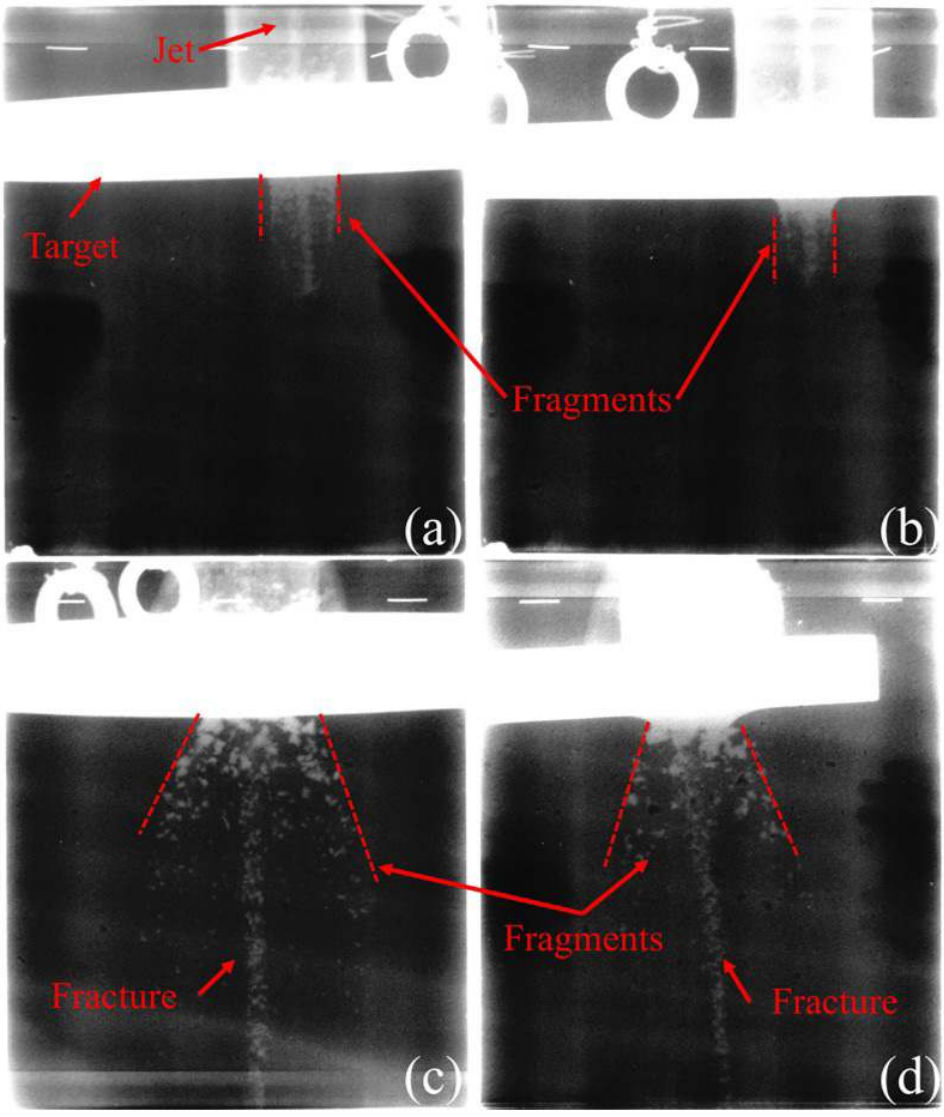

Figure 8 X-ray photos obtained by penetration experiments: (a)54.7μs (b)99.7μs (c)54.8μs (d)99.7μs.

According to the experimental setup, the morphology of the jet after penetrating the targets is captured. The actual emission time T_1 and T_2 in the first experiment are 51.7μs and 99.7μs. In the second experiment, the actual emission time T_1 and T_2 are 54.8μs and 99.7μs. respectively. Figure 8 shows the shape of the jet after penetrating the target. The jet head is consumed during penetration, so it cannot be observed on X-ray photos. However, it can be observed from the Figure 8 (a) and (b) that there are gaps in the jet and the axial fracture trend increases. Compared to 800A, the 1000A jet moves further after penetrating the target, which means that the remaining velocity of the 1000A jet is higher. At this point, the back of the steel target under the impact of the jet, breaks into many small fragments. The direction of fragment dispersion is approximately parallel to the direction of jet motion. The same phenomenon can also be observed at the entrance of the penetration hole. As the distance of jet motion increases (99.7μs), spallation emerges at the back of the steel target under the effect of tensile waves, and large-sized fragments fly outward at larger scattering angles, which will increase the damage range of fragments. The morphology of the remaining jet proves that after the high-speed jet head is consumed during penetration, there is a clear tendency for the remaining jet to fracture. Besides, radial dispersion or expansion is not observed on the jet.

Figure 9 shows the damage of the quilt and oil tank. Experimental results indicate that the jet penetrates the steel target and causes significant damage to the oil tank. There is a large hole and several small holes on the oil tank. The maximum bullet hole on the surface of the oil tank proves that the jet mainly penetrates the oil tank in this direction. Figure 9 (a) shows the damage to the quilt in the first experiment. The high-temperature jet and steel target fragments cause the combustion of quilt contaminated with kerosene. Figure 9 (b), (c), and (d) show the damage of the quilt and oil tank in the second experiment. Shortening the offset distance may cause the oil tank to fall from the platform to the ground due to the impact of fragments and jet. After 15 minutes of the experiment, the quilt on the ground is successfully ignited due to the fire of the kerosene. The burning quilt and oil tank provide conclusive evidence of this process.



Figure 9 Damage of the quilt and oil tank.

In summary, the TiAlVZrNb RHEAs jet still can penetrate the oil tank after penetrating the target. Although jet cannot directly detonate oil tank, they can ignite leaked kerosene on the ground, further triggering fires. The experimental results demonstrate that TiAlVZrNb RHEAs jet has strong aftereffects.

4.3 Numerical simulation verification

4.3.1 Model and parameters

Numerical calculations and analysis are conducted on the jet formation using Autodyn software. The simulation model is shown in Figure 10.

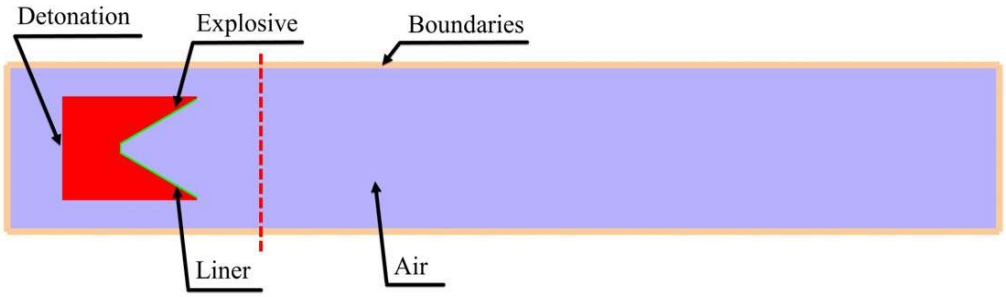

Figure 10 Simulation model.

The overall size of the computational domain is 420mm × 80mm. The grid size of the explosive and liner is 0.2mm × 0.2mm. Located in the air area on the right, the grid size is 0.4mm×0.2mm. Considering the symmetry of the structure, a two-dimensional(2D) symmetric model is established to improve computational efficiency. In this model, the Euler method is used for explosives, liner, and air. The boundaries are set as Flow-out boundaries, and the detonation point is set at the center of the explosive end face.

The constitutive equation of RHEAs adopts the Johnson-Cook model, and the parameters have been given in Section 3.2, which will not be repeated here.

The equation of state (EOS) of TiAlVZrNb RHEAs adopts the Shock EOS. Shock EOS can be described as:

$$U_S = C_0 + S u_P \tag{8}$$

$$\begin{cases} P = P_H + \Gamma \rho (E - E_H) \\ \Gamma = B_0 / (1 + \mu) \end{cases} \tag{9}$$

$$P_H = \frac{\rho_0 C_0^2 \mu (1 + \mu)}{\left[1 - (S - 1)\mu\right]^2} \tag{10}$$

$$\mu = \rho / \rho_0 - 1 \tag{11}$$

where S is a constant and C_0 is the sound speed of the materials; U_S and u_P are the velocity of shock waves and particles, respectively. Γ is the Gruneisen coefficient; B_0 is a constant; μ is compressibility; ρ_0 is the initial density, and P_H is Hugoniot pressure.

In addition, the Hugoniot energy E_H is calculated as:

$$E_H = \frac{P_H}{2\rho_0}\left(\frac{\mu}{\mu + 1}\right) \tag{12}$$

During the jet formation, the aluminum, titanium, and zirconium elements in RHEAs may react with oxygen in the air, releasing energy. However, the rate at which these chemical reactions occur is significantly slower than the time required for the jet formation. Therefore, the RHEAs liner can be regarded as an inert material. Additionally, RHEAs are composed of a mixture of metals. When subjected to an impact load, the pressure between these elements tends to

balance, making the material appear homogeneous. The varying internal energies of each component at equilibrium Hugoniot pressure led to distinct temperatures among them. To address this issue, we can ignore the temperature effect and consider the material to be in a state of thermal equilibrium.

Under the impact load, it is assumed that each component in the mixture instantly reaches pressure equilibrium. The physical parameters in the state equations of each component are interpolated and average based on their atomic fractions:

$$\begin{cases} \Gamma = \sum_{i=1}^{n} m_i \Gamma_i \\ C_0 = \sum_{i=1}^{n} m_i C_i \\ S = \sum_{i=1}^{n} m_i S_i \\ \sum_{i=1}^{n} m_i = 1 \end{cases} \tag{13}$$

where m_i is the atomic fraction of the i-th atom, C_i is the sound velocity of the i-th atom, and S_i is the Gruniesen coefficient of the i-th atom. The composition elements (Selected Hugoniots, 1969) and RHEAs parameters are shown in Table 5 and Table 6.

Table 5 Material properties of components.

Elements	at/%	C_0/(cm/μs¹)	S	Γ
Ti	55	0.5220	0.767	1.09
Al	20	0.5240	1.490	1.97
Nb	15	0.4439	1.207	1.47
V	5	0.5077	1.201	1.29
Zr	5	0.3757	1.018	1.09

Table 6 The EOS parameters of RHEAs.

C_0/(cm/μs¹)	S	Γ
0.5026	1.01	1.33

The EOS for explosive can be described using the Jones Wilkins Lee model (Lee E L. et al. 1968):

$$P_e = A_e(1-\frac{\omega}{R_1 V_e})e^{-R_1 V_e} + B_e(1-\frac{\omega}{R_2 V_e})e^{-R_2 V_e} + \frac{\omega E_e}{V_e} \tag{14}$$

where P_e is the pressure, ρ_e is the density of the explosive, $V_e = 1/\rho_e$ is the relative volume, and E_e is the specific internal energy per unit mass of the explosive. The remaining parameters are constantly obtained by fitting experimental data. The parameters of 8701 explosive are listed in Table 7.

Table 7 Parameters of 8701 explosive.

ρ/(g/cm)	A/GPa	B/GPa	R_1	R_2	ω	V_{CJ}/ (m/s)	P_{CJ}/GPa
1.702	618.4	6.9	4.3	0.87	0.38	8350	29.66

The ideal gas EOS is used to describe air.

$$P = (\gamma - 1)\frac{\rho}{\rho_o}E \tag{15}$$

where γ is the ideal gas constant with a value of 1.4; ρ is the air density of 1.225×10^{-3} g/cm^3, and E is the internal energy per unit mass of air of 206.8 kJ/m^3.

4.3.2 Jet temperature and strength

To verify the accuracy of Johnson-Cook parameters, simulations are conducted on the formation of TiAlVZrNb RHEAs jet. The twenty Gauss points at equal intervals on the inner side of the liner are established to observe the flow state of the liner at different times, as shown in Figure 11. Because the storage interval of simulation result files can affect the accuracy of data, it is necessary to set an appropriate interval to obtain more reliable data. The file save interval is set to 0.1ms in this study.

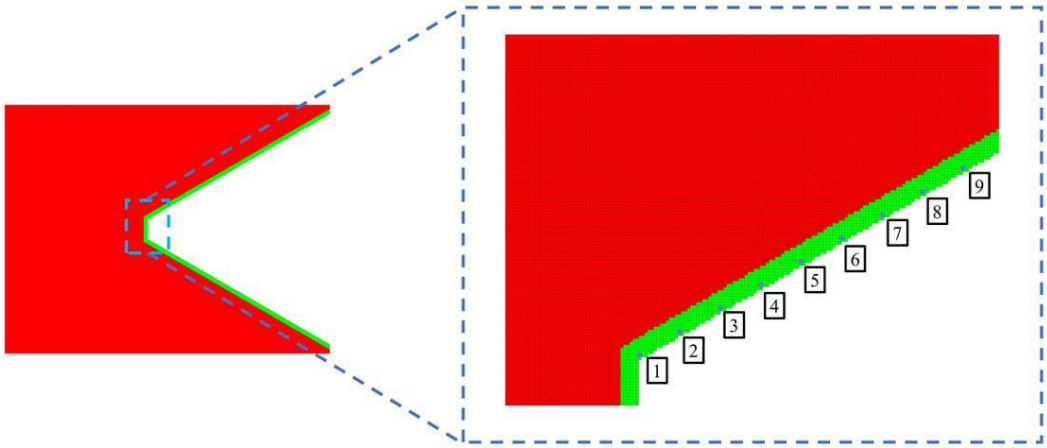

Figure 11 Position distribution of Gauss points.

The numerical simulation results are statistically analyzed, and the characteristic parameters of the jet are shown in Table 8. The relative error (δ) is used to compare the experimental results with the numerical simulation results.

$$\delta = \frac{\left(x^* - x\right)}{x} \times 100\% \tag{16}$$

where x^* is experiment results; x is the numerical simulation results.

After 51μs of detonation, the jet has completed collapse. Currently, the tip velocity of the 1000A and 800A jet are 6812m/s and 6715m/s, respectively. For the jet head velocity and jet length, the maximum error is within 3%, which means that numerical simulation can predict the head velocity and jet length of high entropy alloy jets well. Unfortunately, due to the inability of the Euler algorithm to predict radial dispersion of the jet head, numerical simulations cannot accurately predict the diameter of the jet head.

Table 8 Numerical results of TiAlVZrNb RHEAs jet.

Materials	Time	L_J/mm	D_J/mm	V_J/(m/s)
1000A	51μs	215.2	5.6	6812
δ (%)		+2.91	-49.1	-2.43
800A	52μs	224.8	5.6	6715
δ (%)		-1.57	-48.1	+0.73

The shape of the jet at a calculation time of 52μs is selected as the research object, and the yield strength and temperature distribution relationship at the corresponding Gauss points are statistically analyzed, as shown in Figure 12. The jet can be divided into three parts: the jet tip, the jet body, and the slug. Figure 12 (a) and (c) shows that different Gauss points are in different parts of the jet, with 15% in the slug, 35% in the jet tip, 50% in the jet body. Compared to the slug, the temperature at the jet tip is higher. For the jet body, the temperature near the jet tip is higher. In addition, the yield strength of liner materials is mainly affected by thermal softening strain rate hardening and strain hardening.

Currently, the jet is undergoing tensile deformation, and the strain rate is relatively low, so thermal softening and strain hardening are the main influencing factors. However, the yield strength of all Gauss points is lower than the initial yield strength, indicating that thermal softening dominates. The yield strength of the material decreases due to high temperature.

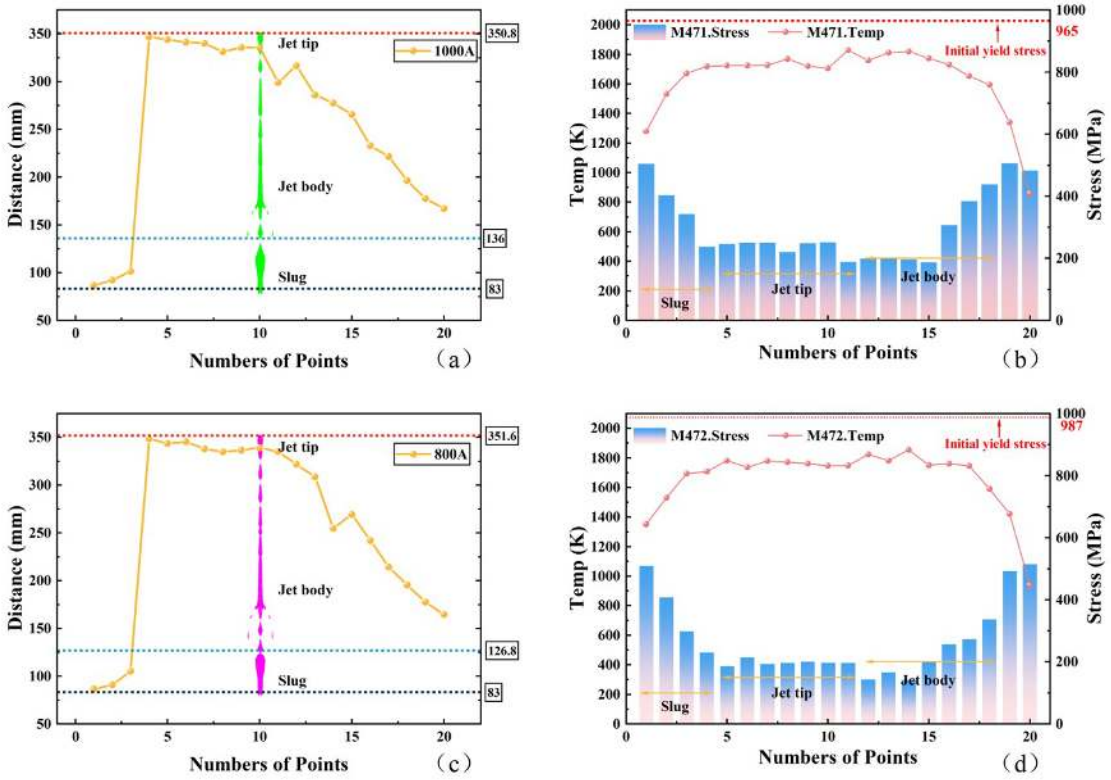

Figure 12 Numerical results of TiAlVZrNb RHEAs jet: (a) Distribution of Gauss Points in 1000A jet (b) Distribution of yield strength and temperature in 1000A jet (c) Distribution of Gauss Points in 800A Jet (d) Distribution of yield strength and temperature in 800A jet

4.4 Jet cohesiveness

The cohesiveness of jets has always been a focus of attention for researchers. Chou et al. (1976) and Walker (1994) established the "sound speed" criterion based on experiments and theoretical research. The collapse angle β and flow velocity V_2 are the key factors affecting the cohesiveness of the jet. In the Table 9, C_L is the sound speed of the liner materials, and β_C is the critical collapse angle.

Compared to calculating β, Shi J. et al. (2023a) have proposed a simpler method. The new method is established by combining PER model (Pugh E M. et al. 1952) and Shock EOS. In the model, pressure is the key influencing factor of jet cohesion. In the Table 10, P_C is the critical pressure, and P_S is the stagnation pressure.

Table 9 Condition for jet cohesion.

Flow regime	Collapse angle	Jet cohesiveness
$V_2 > C_L$	$\beta \le \beta_c$	No
	$\beta > \beta_c$	Yes
$V_2 \le C_L$	All	Yes

Table 10 Condition for jet cohesion.

Flow regime	Critical collapse pressure P_C	Jet cohesiveness
$V_2 > C_L$	$P_S \le P_C$	No
	$P_S > P_C$	Yes
$V_2 \le C_L$	All	Yes

According to the momentum equation, the β can be expressed as:

$$\tan^2\beta = \frac{P\left[\rho_0 V_2^2\left(\frac{\mu}{\mu+1}\right)-P\right]}{\left(\rho_0 V_2^2 - P\right)^2} \tag{17}$$

where ρ_0 is the liner material density.

At $\beta=\beta_c$, $\mathrm{d}\beta/\mathrm{d}\mu = \mathrm{d}/\mathrm{d}\mu\left(\tan^2\beta\right)=0$. Differentiating Eq.(17) yields:

$$\frac{\mathrm{d}P}{\mu} = \frac{P\left[P-\rho_0 V_2^2\right]}{(\mu+1)\left[\mu\rho_0 V_2^2 - P(\mu+2)\right]} \tag{18}$$

Let $V_2 = C_L$, $\Gamma=0$, Eq.(10) can be simplified as:

$$P = \frac{\rho_0 C_L^2 \mu(1+\mu)}{\left[1-(S-1)\mu\right]^2} \tag{19}$$

Differentiating Eq.(19) yields:

$$\frac{\mathrm{d}P}{\mu} = \frac{[1-(S-1)\mu]\rho_0 C_L^2\left\{(2\mu+1)\cdot[1-(S-1)]+2\left(\mu+\mu^2\right)(S-1)\right\}}{[1-(S-1)\mu]^4} \tag{20}$$

According to the results of section 3.2 (*S*=1.01), $S-1\approx 0$. Eq.(20) can be simplified as:

$$\frac{\mathrm{d}P}{\mu} = \rho_0 C_L^2(2\mu+1) \tag{21}$$

Combining Eq.(20) and (18) yields:

$$\frac{P\left[P-\rho_0 V_2^2\right]}{(\mu+1)\left[\mu\rho_0 V_2^2 - P(\mu+2)\right]} = \rho_0 C_L^2(2\mu+1) \tag{22}$$

Solving and substituting Eq.(19) into Eq.(22):

$$\mu(\mu+1)C_L^2 + (\mu+1)(2\mu+1)(\mu+2)C_L^2 - 2(\mu+1)V_2^2 = 0 \tag{23}$$

Due to $\mu+1\neq 0$, Eq.(23) can be simplified as:

$$\mu^2+3\mu+1-\left(\frac{V_2}{C_L}\right)^2 = 0 \tag{24}$$

Critical compression ratio μ_C can be obtained by using Eq.(24):

$$\mu_C = \left(-3 \pm \sqrt{5 + 4 \times \left(\frac{V_2}{C_L} \right)^2} \right) / 2 \tag{25}$$

When the $V_2 / C_L > 1$, μ_C has a positive solution. P_S can be obtained by using Eq.(19). P_S can be obtained by numerical simulation results. Since the radial dispersion of the jet mainly occurs in the jet body and the jet tip, the P_C and P_S corresponding to some Gauss points are compared. The jet head and non-cohesive segment are marked in the Figure 13. The colored area represents the presence of non-cohesiveness in the jet during the formation. At the jet tip, only one gauss point has a P_C greater than P_S. This means that the radial dispersion of jet formation is small.

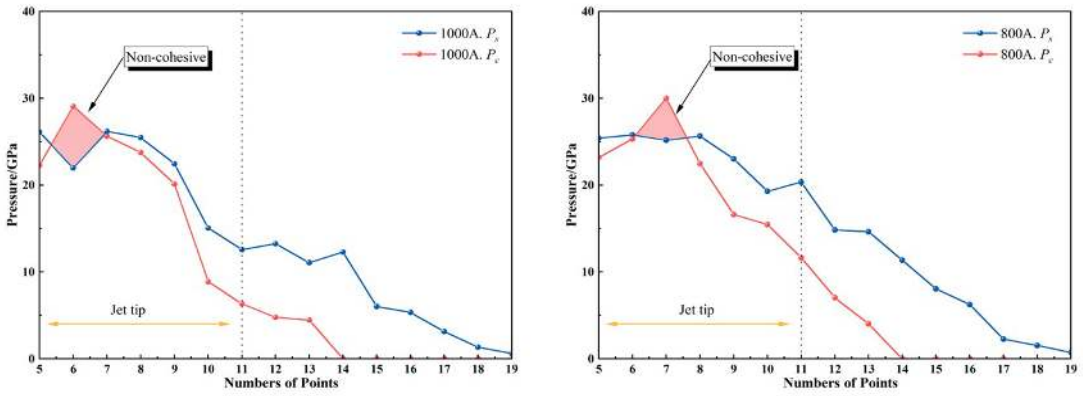

Figure 13 Comparison between critical pressure and stagnation pressure.

Mechanical properties are also important factors affecting jet cohesion. The jet is subjected to high strain rate compression during the collapse. In the collapse, the time is very short, and the liner cannot absorb heat from the outside through heat transfer. The accumulation of heat mainly comes from plastic deformation. However, in collapse, the effect of thermal softening of liner material is far less than that of strain hardening. High strain rates lead to a rapid increase in internal stress of material particles. The mechanical test results show that under high strain rates (4284s^{-1}), the stress at 1000A increases rapidly and the fracture strain decreases sharply (20%). This means that there is almost no plastic deformation in 1000A, which is a manifestation of brittleness. The macro-SEM photos show that the river patterns and cleavage steps on the fracture surface of 1000A specimen can be observed, which are the characteristics of brittle fracture (Wang X. et al. 2022). At this time, the RHEAs materials cannot collapse like copper to form a cohesive jet, but show special brittleness, breaking into particles, and finally forming a particle jet, that is a non-cohesive jet. This means that a brittle metal liner is more likely to form a non-cohesive jet.

However, compared with the traditional titanium alloy jet and amorphous jet (Shi J. et al. 2022, 2023b), the non-cohesive characteristics of TiAlVZrNb RHEAs jet are not obvious. During collapse, the TiAlVZrNb RHEAs liner materials cause plastic deformation in the form of DRX, which improves the cohesion of the jet. However, compared with 1000A, α_2 phase is later than BCC matrix deformation and temperature rise. The difference of mechanical response between the two phases promotes the non-cohesive transition at the end of jet formation (Wang X. et al. 2025).

5 CONCLUSION

This article investigates the quasi-static and dynamic mechanical properties of TiAlVZrNb RHEAs. Based on the tests results, the constitutive parameters of TiAlVZrNb RHEAs are fitted. The morphological evolution and aftereffects of the jet are studied through experiments. The influence factors of jet cohesiveness are discussed. The main conclusions are as follows:

(1) TiAlVZrNb RHEAs have high yield strength and ductility. At a strain rate of 0.001s^{-1}, the yield strengths of 1000A and 800A are 965MPa and 987MPa, respectively. The fracture strain of 1000A exceeds 50%, while the fracture strain of 800A is about 30%. Johnson cook constitutive parameters are fitted based on the test results.

(2) TiAlVZrNb RHEAs liner can form non-cohesive jet. At the end of jet formation, the 1000A jet head has radial expansion characteristics. The 800A jet head has radial dispersion characteristics.

(3) Numerical simulation verified the accuracy of constitutive parameters. The numerical simulation results show that large deformation occurs during the collapse of the high entropy alloy liner. The internal energy during the deformation process causes the temperature of the material to rise, resulting in increased thermal softening and an overall stress level lower than the initial yield strength. Compared to the jet body and slug, the temperature at the jet head is higher and the yield strength is lower.

(4) After penetrating the steel target, TiAlVZNb RHEAs still have enough kinetic energy to penetrate the oil tank and release energy to ignite the quilt. This means that Ti, Al, and Zr elements can improve the aftereffect damage ability of the jet.

ACKNOWLEDGEMENT

The study is funded by Open Research Fund of State Key Laboratory of Target Vulnerability Assessment, Defense Engineering Institute, AMS, PLA (YSX2024KFXY005).

Auhor's Contribuitions: Writing - original draft, Yuanchen Wang; Methodology, Yuanchen Wang; Test technical support, Xudong Zu, Qiangqiang Xiao, Zhengxiang Huang and Xin Jia; Writing - review & editing, Yuanchen Wang and Xudong Zu; Supervision, Qiangqiang Xiao, Xin Jia and Zhengxiang Huang; Funding acquisition, Xudong Zu.

Data availability: Research data is only available upon request.

Editor: Marcílio Alves

References

Cai, Y. E., Tan, Y., Zu, X., Huang, Z., Shen, X., Jia, X., & Xiao, Q. (2024). Study on cone angle of shockwave front in liquid composite protective structure. Latin American Journal of Solids and Structures, 21(3), e537.

Reboul, N., Chinnayya, A., Paintendre, F., Dalle Piagge, S., Jaulin, V., Limido, J., Collé, A., & Rondot, F. (2025). Experimental and numerical study of the interaction between a shaped charge jet and a single ERA moving plate. Defence Technology.

Guo, J., Ma, B., Huang, Z., Peng, Y., & Jia, X. (2024). Simulation and experimental study on the use of shaped charge jet as transient antennas for radiating electromagnetic pulses. Defence Technology.

Kong, C., Li, Y., Jin, Y., Xia, J., Wang, Q., & Liao, Y. (2024). Analysis of the influence of charge liner on the penetration effect of shaped charge jet assisted window sidetracking. Geoenergy Science and Engineering, 243, 213300.

Zhang, X. W., Xiao, Q. Q., Huang, Z. X., Zu, X. D., Jia, X., & Ma, B. (2020). Influence of liner material on penetration capability by jet into high strength concrete. J. Proj. Rocket. Missiles Guid, 40, 1-4.

Guo, J., He, Y., Xiao, Q. Q., Huang, Z. X., & Tan, Y. P. (2017). Influence of yield strength of Ti-alloy liner on crater diameter formed by shaped charge jet penetration. Solid State Phenomena, 263, 30-37.

Niu, Y. Q., Huang, Z. X., Jia, X., Zu, X. D., & Xiao, Q. Q. (2024). Research on the penetration performance of shaped charge jet into block stone concrete targets. International Journal of Impact Engineering, 193, 105060.

Shi, J., Huang, Z. X., Zu, X. D., & Xiao, Q. (2023a). Cohesiveness and penetration performance of jet: Theoretical, numerical, and experimental studies. International Journal of Impact Engineering, 175, 104543.

Han, J. L., Chen, X., Du, Z. H., Fu, H. M., Jing, Y. D., Yuan, T., Chun, C., Du, C. X. & Xu, L. (2019). Application of W/Zr amorphous alloy for shaped charge liner. Materials Research Express, 6(11), 115209.

Shi, J., Huang, Z. X., Zu, X. D., & Xiao, Q. Q. (2022). Experimental Investigation of Zr-Based Amorphous Alloy as a Shaped Charge Liner. Propellants, Explosives, Pyrotechnics, 47(11), e202200063.

Shi, J., Huang, Z., Zu, X., Xiao, Q., & Wang, Y. (2023b). Research on non-cohesive jet formed by zr-based amorphous alloys. Scientific Reports, 13(1), 4149.

Guo, H. G., Zheng, Y. F., He, S., Yu, Q. B., Ge, C., & Wang, H. F. (2022). Reaction characteristic of PTFE/Al/Cu/Pb composites and application in shaped charge liner. Defence Technology, 18(9), 1578-1588.

Wang, H., Guo, H., Geng, B., Yu, Q., & Zheng, Y. (2019). Application of PTFE/Al reactive materials for double-layered liner shaped charge. Materials, 12(17), 2768.

Sun, T., Wang, H., Wang, S., Ge, C., Hu, D., Chen, P., & Zheng, Y. (2024). Formation behaviors of rod-like reactive shaped charge penetrator and their effects on damage capability. Defence Technology, 32, 242-253.

Zheng, Y. F., Zheng, Z. J., Lu, G. C., Wang, H. F., & Guo, H. G. (2023). Mesoscale study on explosion-induced formation and thermochemical response of PTFE/Al granular jet. Defence Technology, 23, 112-125.

Yeh, J. W., Chen, S. K., Lin, S. J., Gan, J. Y., Chin, T. S., Shun, T. T., Tsau, C.H., & Chang, S. Y. (2004). Nanostructured high-entropy alloys with multiple principal elements: novel alloy design concepts and outcomes. Advanced engineering materials, 6(5), 299-303.

Cantor, B., Chang, I. T., Knight, P., & Vincent, A. J. B. (2004). Microstructural development in equiatomic multicomponent alloys. Materials Science and Engineering: A, 375, 213-218.

Senkov, O. N., Wilks, G. B., Miracle, D. B., Chuang, C. P., & Liaw, P. K. (2010). Refractory high-entropy alloys. Intermetallics, 18(9), 1758-1765.

Senkov, O. N., Wilks, G. B., Scott, J. M., & Miracle, D. B. (2011). Mechanical properties of Nb25Mo25Ta25W25 and V20Nb20Mo20Ta20W20 refractory high entropy alloys. Intermetallics, 19(5), 698-706.

Wang, X., Wang, L., Li, T., Jin, K., Wang, B., Li, Y., Sun, S., & Xue, Y. (2022). Precipitation enhancing strain hardening capability of ductile AlTiVZrNb high-entropy alloys upon dynamic loading. Materials Science and Engineering: A, 856, 143964.

Yurchenko, N. Y., Stepanov, N. D., Zherebtsov, S. V., Tikhonovsky, M. A., & Salishchev, G. A. (2017). Structure and mechanical properties of B2 ordered refractory AlNbTiVZrx (x= 0–1.5) high-entropy alloys. Materials Science and Engineering: A, 704, 82-90.

Wang, L., Chen, S., Cao, T., Wang, B., Wang, L., Ren, Y., Liang, J., & Xue, Y. (2021). Lightweight Zr1. 2V0. 8NbTixAly high-entropy alloys with high tensile strength and ductility. Materials Science and Engineering: A, 814, 141234.

Li, T., Wang, X., Wang, B., Jin, K., Liu, X., Wang, L., Zeng, H., & Xue, Y. (2025). Excellent dynamic shear resistance and high dynamic plasticity in TiZrVNbAl multicomponent alloy via high content orthorhombic phase. Journal of Materials Science & Technology, 214, 53-61.

Yan, A. M., Yu, Q., & Dai, L. H. (2022). Formation and stability of shaped charge liner jet of CrMnFeCoNi high-entropy alloy. Chinese Journal of Theoretical and Applied Mechanics, 54(8), 2119-2130.

Chen, J., Liu, T. W., Cao, F. H., Wang, H. Y., Chen, Y., & Dai, L. H. (2022). Deformation behavior and microstructure evolution of CoCrNi medium-entropy alloy shaped charge liners. Metals, 12(5), 811.

Li, R. X., Ding, J. B., Zhao, Y. Y., Tian, Q. W., Zhong, X. T., Wang, R. Q., Song, J. X., Huang J. Y., Wu, J. X., & Li, Y. C. (2024). Preliminary study on the dynamic deformation mechanism of CoCrFeNi high-entropy alloy and its application in the shaped charge liner. Journal of Alloys and Compounds, 999, 175083.

LIU, C., WANG, H., ZHANG, J., & ZHENG, Y. (2024). Research on Behavior of Lightweight High-entropy Alloy Jet Penetrating Concrete Targets. Acta Armamentarii, 45(S1), 60.

Wang, X., Wang, B., Liu, X., Li, T., Zeng, H., Wang, L., Jin, K., & Xue, Y. (2025). Asynchronous deformation behavior of precipitation-hardened high-entropy alloys shaped charge liner under explosive loading. Intermetallics, 176, 108555.

Ren, K., Liu, H., Chen, R., Tang, Y., Guo, B., Li, S., Wang, J., Wang, R., & Lu, F. (2021). Compression properties and impact energy release characteristics of TiZrNbV high-entropy alloy. Materials Science and Engineering: A, 827, 142074.

Chen, C., Tu, Y., Chen, J., & Tang, E. (2023). Dynamic constitutive relationship of TiZrHfCu0. 5 high entropy alloy based on Johnson-Cook model. Journal of Materials Research and Technology, 27, 3729-3740.

Johnson, G. R. (1983). A constitutive model and data for metals subjected to large strains, high strain rates and high temperatures. In Proceedings of the 7th International Symposium on Ballistics, The Hague, Netherlands, 1983.

Selected Hugoniots, Report LA-4167-MS, Los Alamos Scientific Laboratory, Los Alamos, NM,1 May 1969.

Lee, E. L., Hornig, H. C., & Kury, J. W. (1968). Adiabatic expansion of high explosive detonation products (No. UCRL-50422). Univ. of California Radiation Lab. at Livermore, Livermore, CA (United States).

Walker, J. D. (1994, July). Incoherence of shaped charge jets. In AIP Conference Proceedings (Vol. 309, No. 1, pp. 1869-1872). American Institute of Physics.

Pugh, E. M., Eichelberger, R. J., & Rostoker, N. (1952). Theory of jet formation by charges with lined conical cavities. Journal of Applied Physics, 23(5), 532-536.

Dirras, G., Couque, H., Lilensten, L., Heczel, A., Tingaud, D., Couzinié, J. P., Perrière, L., Gubicza, J., & Guillot, I. (2016). Mechanical behavior and microstructure of Ti20Hf20Zr20Ta20Nb20 high-entropy alloy loaded under quasi-static and dynamic compression conditions. Materials Characterization, 111, 106-113.

Lee, W. S., Lin, C. F., & Liu, T. J. (2007). Impact and fracture response of sintered 316L stainless steel subjected to high strain rate loading. Materials characterization, 58(4), 363-370.

Chou, P. C., Carleone, J., & Karpp, R. R. (1976). Criteria for jet formation from impinging shells and plates. Journal of Applied Physics, 47(7), 2975-2981